AIAA JOURNAL
Vol. 46, No. 6, June 2008

Shock-Wave/Boundary-Layer Interaction Control Using Three-Dimensional Bumps for Transonic Wings

H. Ogawa* and H. Babinsky†
University of Cambridge, Cambridge, England CB2 1PZ, United Kingdom
and
M. Pätzold‡ and T. Lutz§
University of Stuttgart, D-70550 Stuttgart, Germany

DOI: 10.2514/1.32049

Three-dimensional bumps have been developed and investigated on transonic wings, aiming to fulfill two major objectives of shock-wave/boundary-layer interaction control, that is, drag reduction and buffet delay. An experimental investigation has been conducted for a rounded bump in channel flow at the University of Cambridge and a computational study has been performed for a spanwise series of rounded bumps mounted on a transonic aerofoil at the University of Stuttgart. In both cases wave drag reduction and mild control effects on the boundary layer have been observed. Control effectiveness has been assessed for various bump configurations. A double configuration of narrow rounded bumps has been found to perform best, considerably reducing wave drag by means of a well-established λ-shock structure with little viscous penalty and thus achieving a maximum overall drag reduction of about 30%, especially when significant wave drag is present. Counter-rotating streamwise vortex pairs have been produced by some configurations as a result of local flow separation. On the whole a large potential of three-dimensional control with discrete rounded bumps has been demonstrated both experimentally and numerically.

Nomenclature

H	=	incompressible shape factor
h_{eff}	=	effective height
M	=	Mach number
p	=	static pressure
p_0	=	total pressure
$\overline{p_0}$	=	overall mass-averaged total pressure downstream of control
$Re_{\delta_1^*}$	=	Reynolds number based on boundary-layer displacement thickness upstream of SBLI
s_B	=	bump spacing in multiple bump configuration
u	=	streamwise velocity
x	=	streamwise coordinate
x_s	=	normal shock position relative to nominal position
y	=	vertical coordinate
z	=	spanwise coordinate
α	=	angle of attack
δ	=	boundary-layer thickness
δ^*	=	boundary-layer displacement thickness
θ	=	boundary-layer momentum thickness or effective deflection angle
ρ	=	density
ω_x	=	streamwise vorticity

Subscripts

a	=	value upstream of convex corner
c	=	control plane limit
i	=	incompressible value
nc	=	value in uncontrolled case
s	=	value of normal shock
1	=	value upstream of SBLI
2	=	value downstream of SBLI
∞	=	freestream value

Presented as Paper 324 at the 45th AIAA Aerospace Sciences Meeting and Exhibit, Reno, Nevada, 8–11 January 2007; received 11 May 2007; revision received 5 January 2008; accepted for publication 5 January 2008. Copyright © 2008 by Hideaki Ogawa, Holger Babinsky, Martin Pätzold, and Thorsten Lutz. Published by the American Institute of Aeronautics and Astronautics, Inc., with permission. Copies of this paper may be made for personal or internal use, on condition that the copier pay the $10.00 per-copy fee to the Copyright Clearance Center, Inc., 222 Rosewood Drive, Danvers, MA 01923; include the code 0001-1452/08 $10.00 in correspondence with the CCC.

*Research Engineer, Aerodynamics Laboratory, Department of Engineering, Trumpington Street. Member AIAA.
†Reader in Aerodynamics, Department of Engineering, Trumpington Street. Asscociate Fellow AIAA.
‡Research Engineer, Aerodynamics Group, Department of Aerodynamics and Gas Dynamics.
§Research Engineer, Aerodynamics Group, Department of Aerodynamics and Gas Dynamics. Member AIAA.

I. Introduction

SHOCK-WAVE/boundary-layer interactions (SBLIs) take place on transonic wings of passenger transport, significantly affecting the aerodynamic performance and limiting the operational range. This remarkable impact has attracted much attention of aerodynamicists for the last few decades and brought about a wide variety of shock control methods. In principle, shock control techniques aim at reduction of drag and suppression of flow breakdown or buffet. Drag reduction in the high-speed regime can typically be achieved by producing a bifurcated shock structure in the presence of control as shown in Fig. 1. This so-called λ-shock structure can reduce the impact of shock waves by replacing a single normal shock wave with several shock legs. This reduces wave drag because the total pressure loss through a series of oblique shock waves is always smaller than across a normal shock wave with the same pressure jump. A λ-shock structure can be introduced by deflecting the near-wall flow by means of pneumatic effects with air injection or surface geometry variations. Figure 2 shows a typical distribution of surface pressure with and without such control. At the onset of control, the surface pressure experiences an initial pressure rise across the leading shock leg, followed by a plateau in the λ region. The rear shock leg enables the flow to achieve the same pressure jump as the uncontrolled case. Consequently, overall drag reduction can be achieved, unless the boundary layer suffers from significant viscous penalty.

Examples of control techniques hitherto developed include vortex generators, oscillatory control, discrete suction, discrete blowing, passive control, active control, hybrid control, and mesoflap control [1–6]. All of these techniques attempt to achieve one or more of the

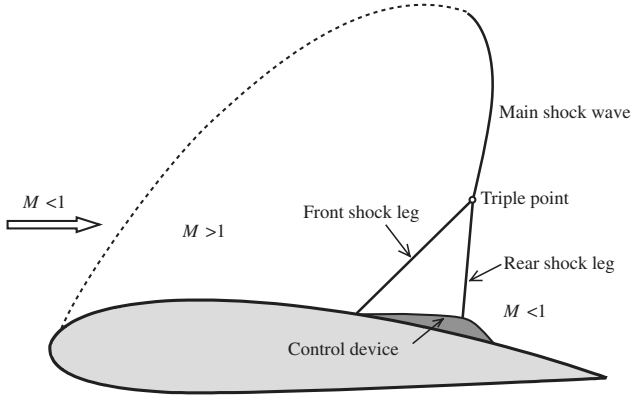

Fig. 1 Transonic aerofoil with control.

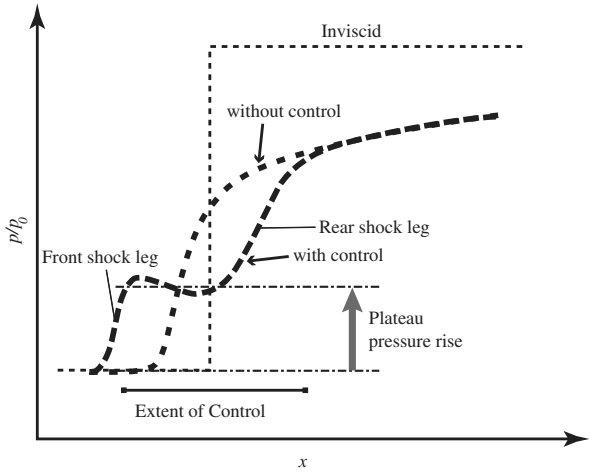

Fig. 2 Surface pressure distributions with/without control.

aforementioned objectives, that is, reduction of drag and suppression of flow breakdown or buffet, but unfortunately, none have been successful in achieving both. Various researchers in the extensive project EUROSHOCK II [7] report that a more direct way of deflecting the near-wall flow, namely, surface bump control, when tuned appropriately, can effectively reduce overall drag owing to λ-shock benefits with little viscous penalty. Two-dimensional bumps have demonstrated favorable drag reduction at design points, but also undesirable drag penalties under off-design conditions.

Recent studies [8–12] have demonstrated that three-dimensional devices such as streamwise slots, grooves, and bumps can introduce a global λ-shock structure with local flow deflection, incurring less installation cost when compared to traditional two-dimensional techniques. Detrimental effects on the boundary layer are confined to the immediate vicinity of the device. Under certain conditions, streamwise vortices are generated by such devices and this is thought to have the potential to reduce shock-induced separations and delay buffet onset. However, most of the devices investigated in their studies were found to be unable to reduce drag due to insufficient control effect or detrimental flow features.

Holden [13] reported that shock waves became increasingly unstable when testing various methods of shock control in a conventional simple working section. This problem was recently elucidated and a new working section was contrived [14], which can successfully overcome this instability.

The new working section has enabled the investigation of novel three-dimensional bumps, which are expected to be beneficial in reducing total pressure losses by producing a global λ-shock structure and suppressing separation by inducing streamwise vortices. This paper presents the results of research on a variety of three-dimensional bumps, based on extensive experimental studies undertaken at the University of Cambridge [15]. Numerical studies have also been conducted at the University of Stuttgart [16,17] to verify and control effects of three-dimensional bumps on a transonic wing in the presence of surface curvature.

II. Experimental Arrangements

A. Measurement Techniques

The experimental investigation was performed in the blowdown-type supersonic wind tunnel of the University of Cambridge. The cross section of the working section is 114 mm wide and 178 mm high (see Fig. 3). The total temperature is 297 K. The total pressure is 2.1×10^5 Pa at $M_1 = 1.3$. x, y, and z are the streamwise, vertical, and spanwise coordinates, respectively. The origins of the coordinates are 86 mm downstream of the nozzle end, the tunnel floor, and the centerline, respectively. Static pressures are measured through pressure tappings located on the floor of the wind tunnel by transducers. Total pressures are measured upstream of the control region at $x = -30$ mm with a flat-head pitot probe and downstream at $x = 76$ mm by means of boundary-layer and freestream traverse employing four-head rake-type pitot probes placed in a row vertically. Distributions of the static and total pressures are mirrored about the wind-tunnel centerline, assuming flow symmetry. Shock positioning is stably performed by employing a shock-holding plate and a choking flap which can accurately adjust the shock standoff distance (see [14] for details). The Mach number is calculated with the isentropic relations in subsonic flows and the Rayleigh pitot-tube formula in supersonic flows. The velocity is calculated with the total pressure and the local wall static pressure. The boundary-layer thickness is determined by means of a curve-fitting method proposed by Sun and Childs [18] for attached boundary layers. In the case of separated boundary layers, the boundary-layer edge is defined at the point where the velocity recovers to 99.5% of the freestream value.

B. Measurement Accuracy

Measurement uncertainties are estimated by means of the partial differential method [19]. Only the precision error is considered here, because the bias error can be estimated only with the aid of more accurate instruments, which were unavailable for most quantities, and it is thought to be by far smaller than the precision error in the measured quantities. The errors in the measurement of static and total pressures are estimated to be ±0.6% and ±0.8%, respectively. This introduces errors in Mach number and velocity of ±0.6% and ±3% for inflow and downstream of SBLIs, respectively. Consequently the error in mass-averaged total pressure $\overline{p_0}$ is estimated to be ±1%. The boundary-layer parameters can bear uncertainties of ±1% in thickness δ, ±4% in displacement thickness δ^*, ±2% in momentum thickness θ, and ±3% in incompressible shape factor H_i. The uncertainty associated with the traverse gear can introduce an additional error of ±1% to these thicknesses. A detailed discussion of uncertainties and their sources can be found in [15].

C. Control Devices

A number of three-dimensional bumps with rounded corners have been designed, based on the wedge bump. The length and angle of bumps have been parameterized to facilitate comparison of control effects.

Figure 4 shows the bump geometry and the nominal position of the normal shock $x_s = 0$. Tabulated in Table 1 are the values which define each bump shape. The flanks are represented by a cosine function to ensure smooth jucntions at any edge with the tunnel floor. The other parameters are constrained by the following relations: $a_1 = e_1$, $a_4 = e_3$, $e_1 = w_1/2$, $e_2 = w_2/2$, $e_3 = w_3/2$, $r_1 = a_1/\tan\frac{\theta_1}{2}$, $r_2 = a_2'/\tan\frac{\theta_1}{2}$, $r_3 = a_3'/\tan\frac{\theta_2}{2}$, and $r_4 = a_4/\tan\frac{\theta_2}{2}$, where $a_2' = a_2/(1+\cos\theta_1)$ and $a_3' = a_3/(1+\cos\theta_2)$, apart from the wedge bump where all of these parameters are set to be zero to shape angular corners. Figure 5 displays bump models generated by the above definitions.

The surface of rounded bumps inherently comprises small steps due to multiple layers, typically 20 layers in a bump of 5.25 mm high. These are a result of the rapid-prototyping manufacturing process.

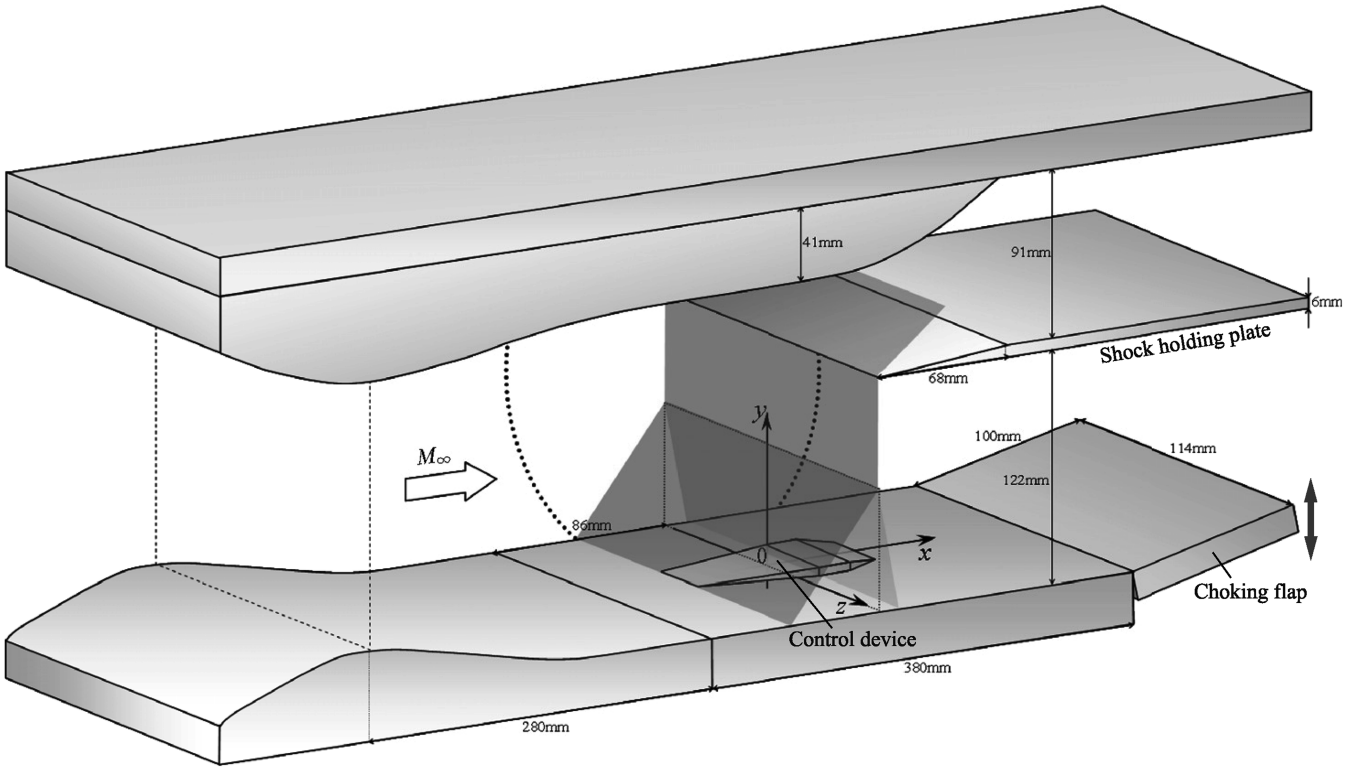

Fig. 3 Schematic diagram of wind-tunnel working section.

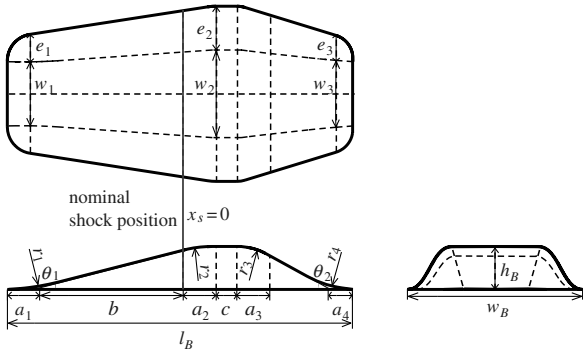

Fig. 4 Definition of bump geometry and nominal shock position.

One exception is the default rounded bump (or just referred to as the "rounded bump" from here on), where the surface was smoothed with filler and sandpaper. Because of budgetary constraints it was not possible to treat all bump shapes in this manner. The influence of surface roughness on the control effectiveness is discussed in Sec. V.A. The impact of roughness on SBLIs has been found to be rather small with respect to the λ-shock structure and its benefits, although there is a small viscous drag penalty. The use of rough surfaces is not expected to invalidate the results of the current research, as it may well be argued that bumps with smooth surfaces would bring about even greater control benefits than those presented here. A more detailed discussion of the effects of a rough surface can be found in [15].

III. Computational Arrangements

A. Computational Method

The computational investigation was conducted with the vectorized and parallel NEC SX-8 supercomputer of the High Performance Computation Centre at the University of Stuttgart. Use was made of the FLOWer code [20], which solves the Reynolds-averaged Navier–Stokes (RANS) equations for three-dimensional compressible flow fields with the finite volume approach. Time integration toward the steady state is accomplished by an explicit five-stage Runge–Kutta scheme with the aid of local time stepping and a multigrid method to accelerate convergence. The RANS equations are closed by employing the shear-stress-transport model [21], a two-equation eddy-viscosity turbulence model.

B. Computational Setup

A numerical study has been conducted with a DA VA2 turbulent-type aerofoil to investigate the control effects in a transonic flow controlled with a series of default rounded bumps. The characteristics of such a flow may well differ from that seen in channel-flow experiments; the shock position can vary on a transonic aerofoil, depending on the flow condition, and the λ-shock structure lies on a curved surface, whereas it stands on a flat surface at a fixed streamwise position in the channel-flow experiment. Therefore it is

Table 1 Parameters of three-dimensional bumps (mm)

Bump shape	θ_1	θ_2	b	c	w_1	w_2	w_3	a_2	a_3	l_B	w_B	h_B
Wedge bump	5 deg	12 deg	60	15	20	30	20	0	0	100	30	5.2
Long wedge bump	5 deg	5 deg	60	15	20	30	24	0	0	135	30	5.2
Default rounded bump	5 deg	12 deg	50	10	20	30	20	10	10	118	60	4.8
High rounded bump	10 deg	23 deg	50	10	20	30	20	10	10	118	60	9.7
Narrow rounded bump	5 deg	12 deg	50	10	10	15	10	10	10	108	30	4.8
Long rounded bump	5 deg	6 deg	50	10	10	30	20	10	10	140	30	4.8

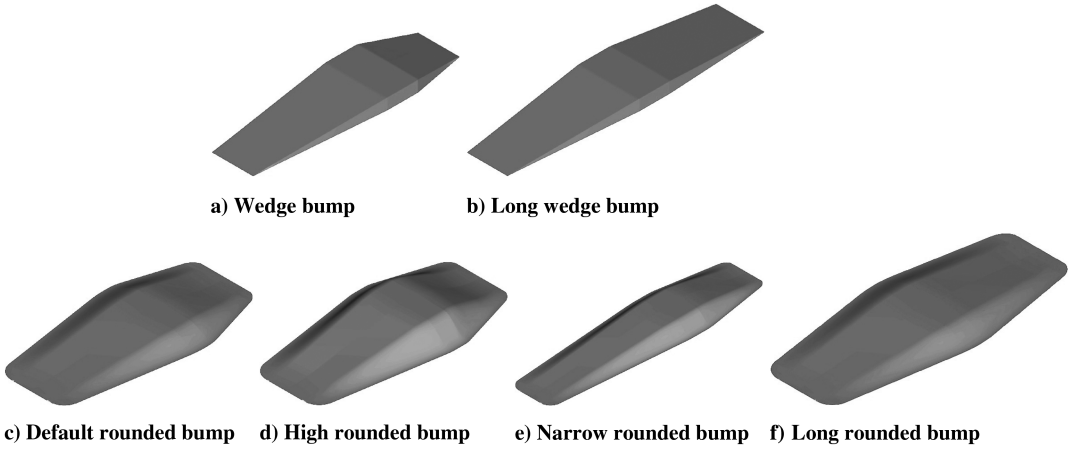

a) Wedge bump b) Long wedge bump

c) Default rounded bump d) High rounded bump e) Narrow rounded bump f) Long rounded bump

Fig. 5 Three-dimensional bumps.

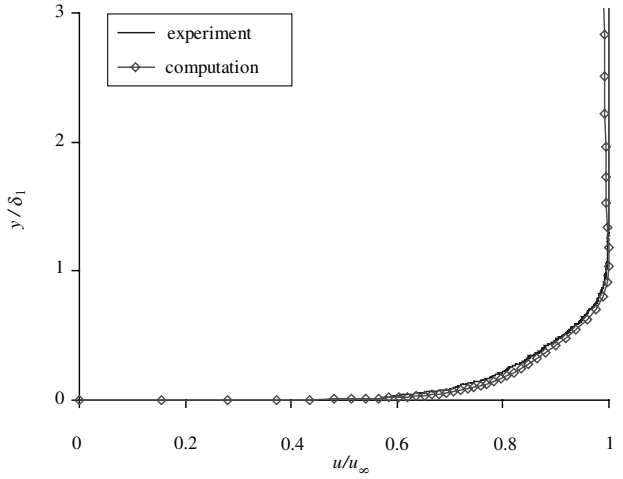

Fig. 6 Inflow velocity profiles (uncontrolled SBLI, $x = -30$ mm).

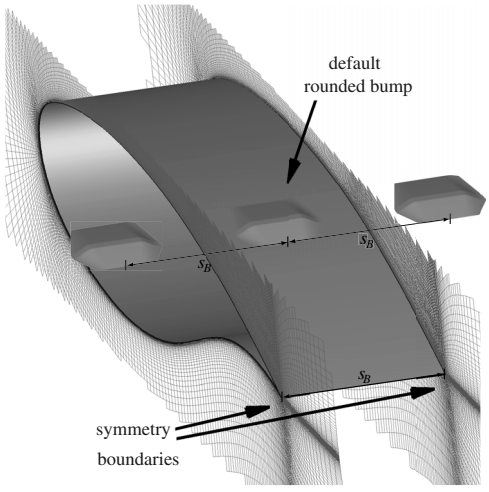

Fig. 7 Computational setup on transonic aerofoil.

of particular interest here to compare the effects of bump control between experiment and computation from a practical point of view in consideration of the application to a real aircraft, for which it is essential to ensure agreement of the inflow condition. As a result of initial parametric calibration, the freestream Mach number and the angle of attack were set to be $M_\infty = 0.76$ and $\alpha = 0.8$ deg to yield the best baseline agreement. The velocity profiles are plotted and compared in Fig. 6, nondimensionalized by the freestream velocity and the inflow boundary-layer thickness. The somewhat fuller boundary layer and a slight declination of freestream velocity in the computation can be attributed to curvature and boundary-layer history effects on the aerofoil. Under these conditions, the Mach number and the boundary-layer parameters match very closely upstream of SBLIs, as seen in Table 2. The default rounded bump has been employed to investigate control effects in comparison with experiment. Periodic boundary conditions by means of symmetry boundaries have been applied to simulate a spanwise series of bumps mounted on the infinite wing with a fixed spacing, as shown in Fig. 7. Similar to the experiment, the spacing has been set to be $100\delta_1^*$. This has been obtained by subtracting two displacement thicknesses from the wind-tunnel channel width, which effectively accounts for the domain free from side-wall effects. The Reynolds number based on the aerofoil chord length is 2.0×10^7 and transition to turbulent flow has been imposed at 10% chord length from the leading edge on the aerofoil. The employed computational code as well as the computational mesh have been evaluated in numerous preliminary runs and its capability of capturing shock-induced separation has been validated with the well-known RAE-2822 aerofoil case [17].

Table 2 Characteristic flow parameters upstream of SBLI

	M_1	δ_1, mm	δ_1^*, mm	θ_1, mm	H_{i1} (H_1)	$Re_{\delta_1^*}$
Experiment	1.30	7.13	1.04	0.54	1.27 (1.94)	33,000
Computation	1.30	6.98	1.08	0.52	1.30 (2.08)	33,700

IV. Results

A. Wedge Bump

A wedge bump has been examined initially to acquire fundamental characteristics of SBLIs controlled by three-dimensional bumps. Figure 8a shows a schlieren image of a SBLI in the absence of control. (The deflection of the tunnel floor is an optical effect of the schlieren system. The thin oblique lines impinging on the normal shock represent spurious Mach waves which emanate from gaps between wind-tunnel parts and are thought to have little impact on SBLIs.) Compression waves are seen at the shock foot, which is a typical feature of unseparated SBLIs. The boundary layer thickens across the shock wave. Schlieren visualization of SBLIs controlled with the wedge bump are presented in Figs. 8b–8d for shock positions $x_s = -25$, 0, and 25 mm, respectively. It is found that the front shock position $x_s = -25$ mm (Fig. 8b) produces a small λ-shock strucure accompanied by auxiliary minor λ-type shock systems at the sharp convex corners due to flow acceleration by reexpansion. On the other hand, the rear shock position $x_s = 25$ mm (Fig. 8d) gives rise to a notable reexpansion region at the rear edge of the bump crest, significantly offsetting any benefits from a large λ-shock structure. The middle shock position $x_s = 0$ mm (Fig. 8c), where the rear shock foot is located exactly at the leading

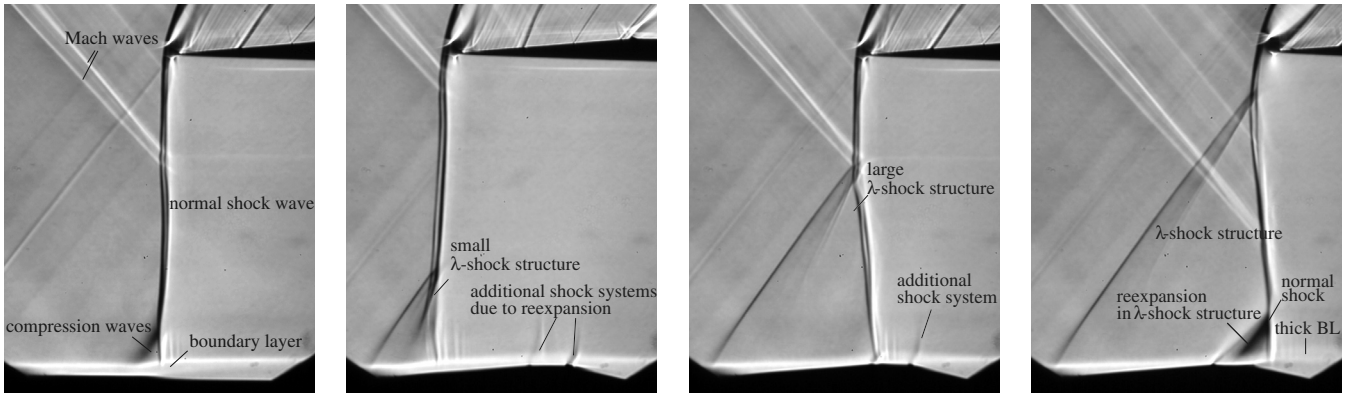

a) No control **b) Wedge bump (x_s=−25mm)** **c) Wedge bump (x_s=0mm)** **d) Wedge bump (x_s=25mm)**

Fig. 8 Schlieren visualization.

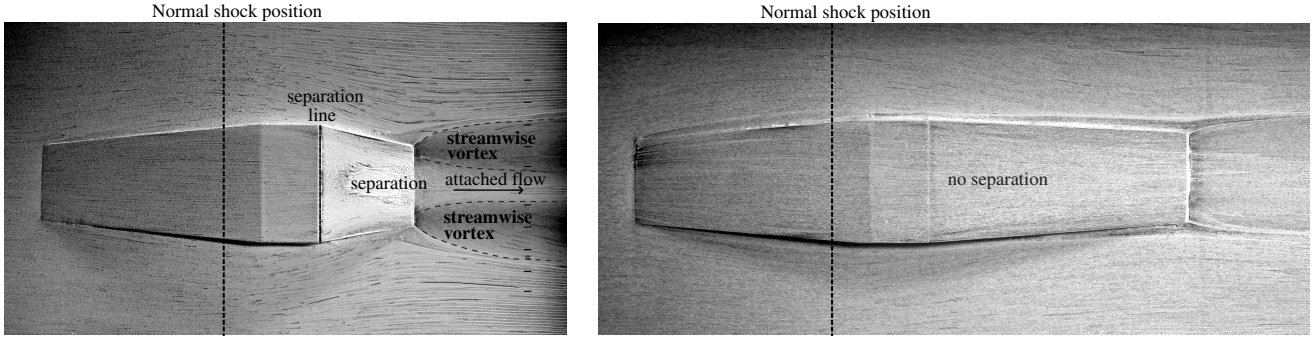

a) Wedge bump **b) Long wedge bump**

Fig. 9 Oil flow visualization ($x_s = 0$ mm).

edge of the bump crest, generates a large λ-shock structure, but secondary shock systems are still observed at the rear edge of the bump crest. The development of these flow structures depending on the shock position is discussed in Sec. V.

A surface oil pattern of a flowfield controlled with the wedge bump is shown in Fig. 9a for the middle shock position $x_s = 0$ mm. Streamwise vortices can be observed behind the bump. Flow separation is indicated by oil accumulation on the rear slope, but the direction of streamlines between vortices suggests flow reattachment a short distance downstream of the bump end. Figure 9b shows an oil flow pattern in the presence of a wedge bump with a long tail and hence a gentle back slope. No indication of flow separation can be observed here. Therefore it can be concluded that the separation observed with the original wedge bump has been caused by the steep rear ramp angle. This is in agreement with the empirical criterion by Chung [22], who suggests the transonic convex corner flows separate when $M_a^2\eta$ is greater than 8.95, where M_a is the Mach number just upstream of a convex corner and η is the ramp angle in degrees. In the current study $M_a^2\eta$ is 14.0 and 5.83 for the original and long wedge bumps, respectively.

B. Default Rounded Bump

To prevent sharp corners, a default rounded bump has been designed, based on the wedge bump. Figure 10a shows the flow on this bump for a shock located at $x_s = 0$ mm. A λ-shock structure whose front shock leg starts at the leading edge of the bump can be seen. However, at the rear shock foot is a small pseudo-λ-shock structure. This is thought to be caused by reacceleration of the flow on the convex curvature at the bump ridge, leading to reduced total pressure recovery. The oil flow pattern shown in Fig. 10c indicates the presence of a vortex pair and a separation bubble. A considerable deficit of total pressure has been observed downstream of the pseudo-λ-shock structure and as a result of the thickened boundary layers [15]. A slight upstream movement of the shock position to $x_s = -10$ mm has improved the situation, eliminating the pseudo-λ-shock structure, as seen in Fig. 10b. The oil flow pattern (Fig. 10d) shows attached flow at the centerline and a trace of a vortex pair behind the bump shoulders. This result suggests that some drag penalties are likely to be incurred, when the shock wave moves downstream beyond its design point. However, this needs to be investigated in the context of the flow over an aerofoil, which is out of the scope of the present study.

Figure 11 compares the surface pressure distributions on the default rounded bump from the channel-flow experiment and computation on a DA VA2 aerofoil. (Note that the bump shape superimposed here is smaller than the specification given in Table 1 as a result of manufacture and surface smoothing. Computation has adopted the specification of the default rounded bump which was actually used in experiment.) On the whole, similar trends can be observed in both cases: the surface pressure undergoes a mild rise at the leading edge of the bump across the front shock leg and then increases considerably across the rear shock leg. The streamlines computed on a transonic aerofoil surface in Fig. 11b show two vortex pairs downstream of the shock. This suggests the presence of flow separation behind the bump shoulders on a transonic aerofoil more distinctly than in the experimental results (Fig. 10d). The difference in the degree of separation is yet to be scrutinized, but may be attributed to curvature effects and greater downstream pressure recovery on the aerofoil, limitation of the turbulence model in capturing separation and reattachment, or side-wall effects in experiment.

Figure 12a displays the Mach number distribution on the center plane $z = 0$ mm in the proximity of the default rounded bump on the DA VA2 aerofoil. Seen in the controlled region is a λ-shock structure introduced by the flow deflection on the surface, in line with the schlieren image in Fig. 10b. It can also be observed that the Mach number is almost uniform in the λ region between the two shock legs

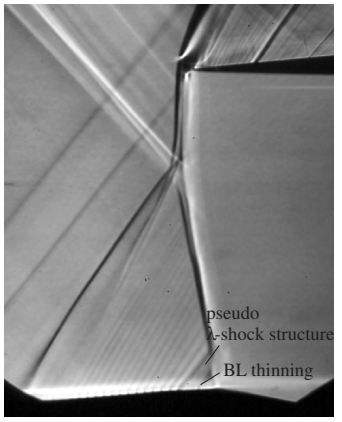

a) Schlieren photo (x_s = 0mm)

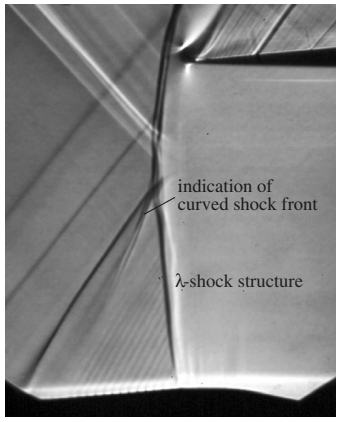

b) Schlieren photo (x_s = −10mm)

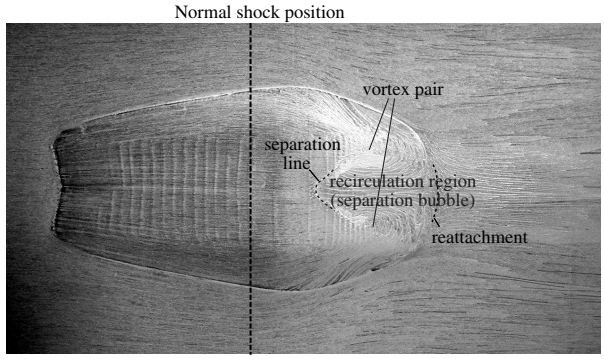

c) Oil flow pattern (x_s = 0mm)

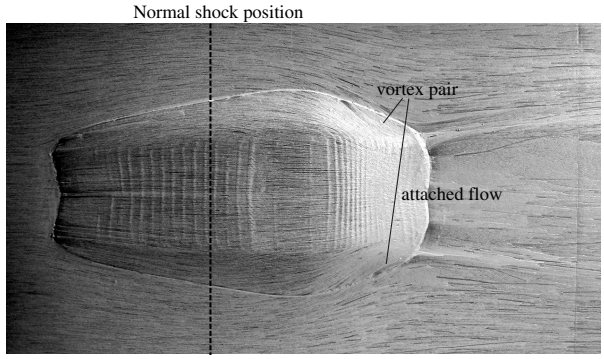

d) Oil flow pattern (x_s = −10mm)

Fig. 10 Flow visualization (default rounded bump).

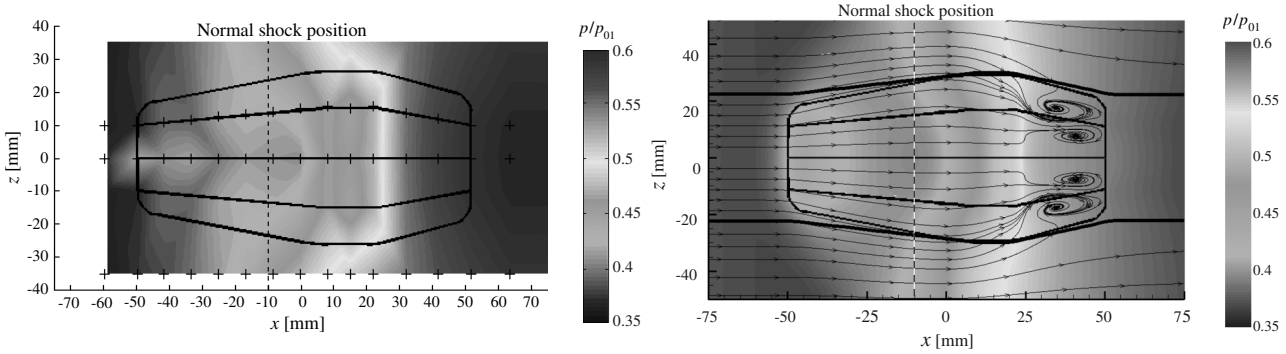

a) Experiment (channel flow) b) Computation (DAVA2 aerofoil)

Fig. 11 Surface pressure distributions and streamlines (default rounded bump, $x_s = -10$ mm).

and the supersonic domain is terminated across the normal shock and the rear shock leg. The streamwise vorticity computed on the DA VA2 aerofoil is plotted in Fig. 12b at $x = 76$ mm. The distribution confirms the presence of two pairs of counter-rotating vortices, in line with the observation in Fig. 11b. It is notable that primary streamwise vortex pairs are confined to a region immediately downstream of the bump ($y \leq 7$ mm and -20 mm $\leq z \leq 20$ mm) and that a secondary vortex pair exists in outer regions. This suggests that the wake spreads little in wall-normal or spanwise directions.

Distributions of the boundary-layer parameters downstream of the rounded bump are plotted in Fig. 13a. Generally, they are comparable to the values observed without control and there is little spanwise variation. (Uncontrolled values are measured at $x =$ 76 mm with a normal shock positioned at $x_s = 0$ mm.) This confirms an absence of streamwise vortices due to separation in agreement with the oil flow visualization in Fig. 10c. The total pressure distributions downstream of SBLIs are plotted in Fig. 13b along with the uncontrolled case. Fairly uniform total pressure distributions can be seen in the spanwise direction. There are appreciable total pressure savings owing to bump control as a result of the generation of a λ region, whereas only very mild effects on the boundary layers are seen at all measured positions.

The computational study has demonstrated a gain in the lift-to-drag (L/D) ratio of 5.26% on a transonic wing. Further gain would be expected if separation were removed. However, particular care ought to be taken in the bump design for transonic wings, because reducing bump height might well suppress separation at the cost of reduction in total pressure savings due to a smaller λ-shock structure. Control effects as well as the influence of streamwise vortices as a result of separation on lift requires careful consideration in the discussion of the performance of bump control on transonic wings. These are beyond the scope of the present study and will be discussed in a following paper [23] and [17].

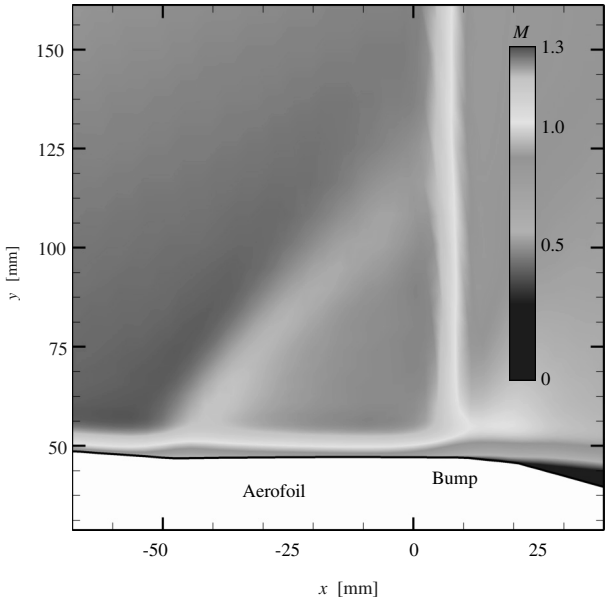

a) Mach number

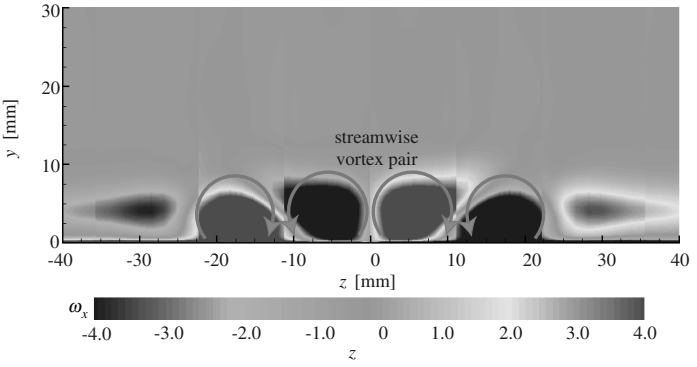

b) Streamwise vorticity

Fig. 12 Distributions of Mach number and streamwise vorticity on DA VA2 aerofoil (default rounded bump, $x_s = -10$ mm, computation).

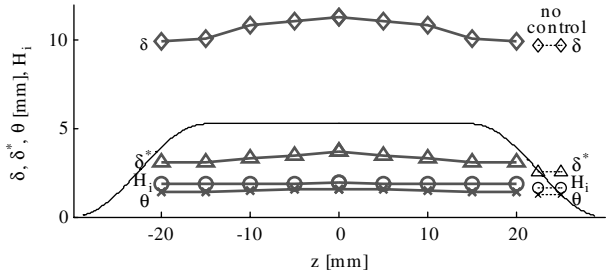

a) Boundary-layer parameters

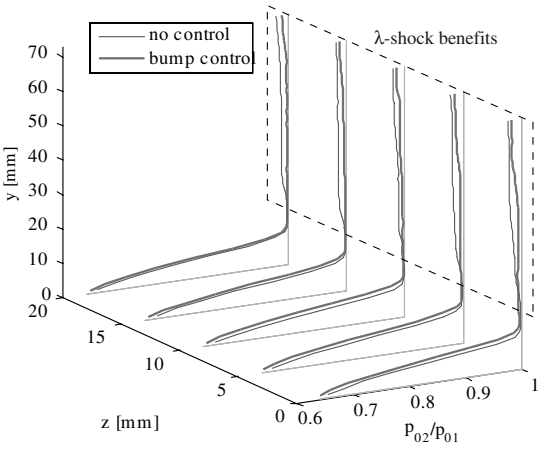

b) Total pressure

Fig. 13 Distributions of boundary-layer parameters and total pressure (default rounded bump, $x_s = -10$ mm, experiment).

C. High Rounded Bump

A rounded bump with a greater height has been examined to investigate the potential of a stronger control effect. A schlieren image of this flow is shown in Fig. 14a. A larger flow deflection is indicated by a greater shock angle of the front shock leg. This has resulted in a remarkably high total pressure recovery behind the λ region, as shown later in Fig. 17. However, a skewed secondary λ-shock system can be seen behind the λ-shock structure. This is

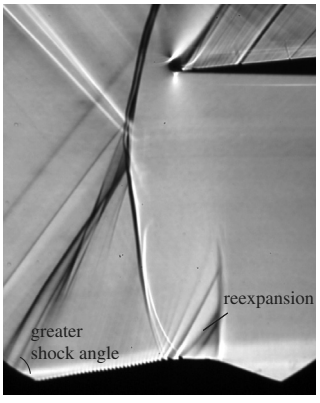

a) Schlieren photo

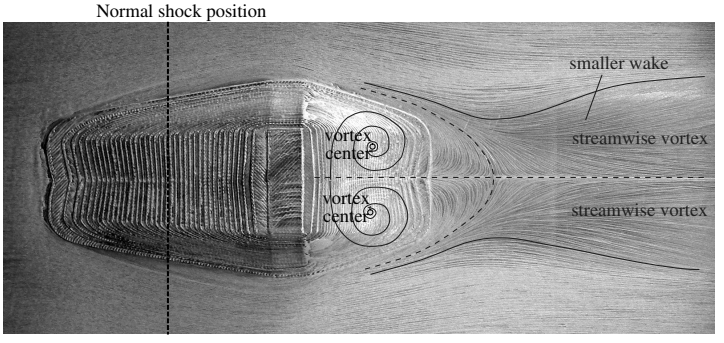

b) Oil flow pattern

Fig. 14 Flow visualization (high rounded bump, $x_s = -20$ mm).

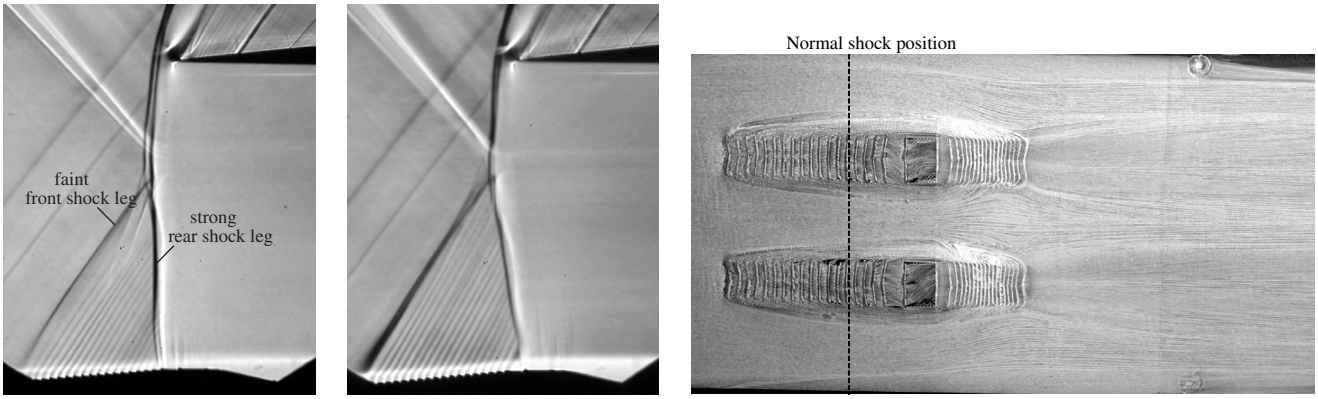

a) Schlieren photo (single configuration)

b) Schlieren photo (double configuration, $s_B = 40$mm)

c) Oil flow pattern (double configuration, $s_B = 40$mm)

Fig. 15 Flow visualization (narrow rounded bump, $x_s = -10$ mm).

associated with the existence of a supersonic region downstream of the primary λ-shock structure due to reexpansion. The oil flow pattern in Fig. 14b visualizes the flowfield on the surface. It clearly indicates the presence of a pair of streamwise vortices in the downstream region which originates from vortex centers found at the rear of the bump. These vortices are found to be confined to a relatively narrow region in the wake, but the presence of separation nevertheless incurs a viscous drag penalty.

D. Narrow Rounded Bump

To investigate the influence of the cross-sectional area on the control effect, rounded bumps with half the width of the default bumps have been examined in single and multiple configurations. Shown in Figs. 15a and 15b are schlieren photographs of SBLIs in the presence of a single bump and two bumps separated by a distance $s_B = 40$ mm in the spanwise direction. Front shock legs with a nearly identical shock angle can be seen in both cases, but the single bump configuration (Fig. 15a) appears to have a relatively weak front shock leg and a nearly normal strong rear shock leg, in contrast to the double bump configuration (Fig. 15b). This suggests smaller flow deceleration across the front shock leg and hence relatively small effectiveness of control in the single bump case. The high effectiveness of multiple bump configurations in terms of total pressure recovery across the λ region is discussed in Sec. V. The surface oil pattern in this case is shown in Fig. 15c, indicating attached flow and little interference between adjoining bumps in the downstream region. The spanwise distributions of the total pressure downstream of SBLIs demonstrate a highly two-dimensional λ-shock structure in multiple bump configurations [15].

V. Discussion of Results

A. Control Effectiveness

The performance of three-dimensional bumps can be evaluated with respect to total pressure recovery and average boundary-layer thickness, which act as indicators for wave drag and viscous drag, respectively. Furthermore, mass-averaged total pressure is employed to evaluate overall drag reduction. The bumps assessed here also include an unsmoothed rounded bump with rough surface as well as further geometry variations in length, height, and width and multiple bump configurations. Detailed results for these bumps are not presented in this paper but can be found in [15,24].

1. *Total Pressure Recovery*

SBLI control with a λ-shock structure primarily relies on the principle that the total pressure recovery through two shock legs is greater than across a single normal shock. Therefore the total pressure recovery behind the λ region serves as a direct indicator of the λ-shock effect. Its variation with respect to the front shock deflection angle θ is analytically calculated and plotted in Fig. 16 on the assumption that the front shock is a weak solution to the oblique shock relations and the rear shock leg is a normal shock [25]. It can be seen that the maximum total pressure recovery $p_{02}/p_{01} = 0.997$ can be achieved at $\theta = 4.9$ deg, equivalent to an 86% reduction in total pressure loss. Although most of the bumps investigated here are designed to have a front slope with a deflection angle (θ_1 in Fig. 4) of about 5 deg, hence near the optimum, their overall effect is expected to be below this value due to relieving effects as a result of their three-dimensional shape. However, the current study as well as previous research [8–11,13,15] suggests that a λ-shock structure generated by three-dimensional devices relaxes only slowly in the spanwise direction. Nevertheless, the effective deflection angle of a three-dimensional bump is always below the geometric value due to viscous relieving effects.

The total pressure ratio behind bump control at the wind-tunnel centerline is plotted in Fig. 17. It can be seen that most configurations have produced respectably high total pressure recovery as a λ-shock benefit, owing to fairly two-dimensional λ-shock structures. The high rounded bump shows a remarkably large value close to the maximum possible value calculated above, that is, it is nearly isentropic. It can also be noted that double configurations have brought about comparably high total pressure recovery.

2. *Mass-Averaged Total Pressure*

The mass-averaged total pressure is a parameter commonly employed to evaluate the performance of shock control. Integration over the control plane (the control plane extends at $x = 76$ mm over an area covered by total pressure measurement in experiment, which is typically $y = 0$–73 mm, $z = 0$–20 mm for single, and $z = 0$–30 mm for double bump configurations) gives the overall mass-averaged total pressure as follows:

$$\overline{p_0} \equiv \frac{\int_0^{z_c}\int_0^{y_c} \rho u p_{02}\,\mathrm{d}y\,\mathrm{d}z}{\int_0^{z_c}\int_0^{y_c} \rho u\,\mathrm{d}y\,\mathrm{d}z} \tag{1}$$

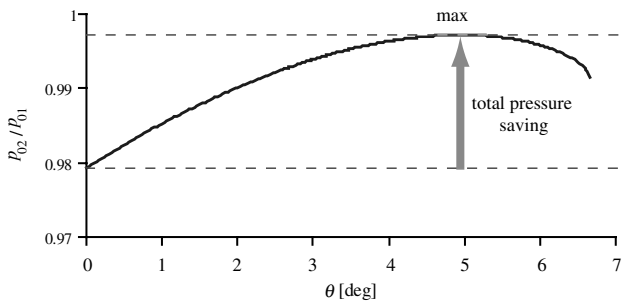

Fig. 16 Total pressure recovery with deflection angle variation ($M_\infty = 1.3$).

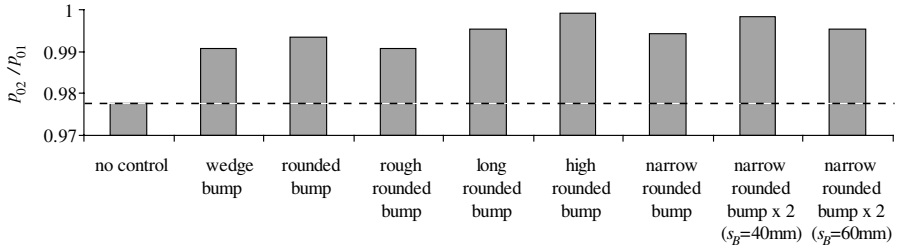

Fig. 17 Total pressure recovery at centerline.

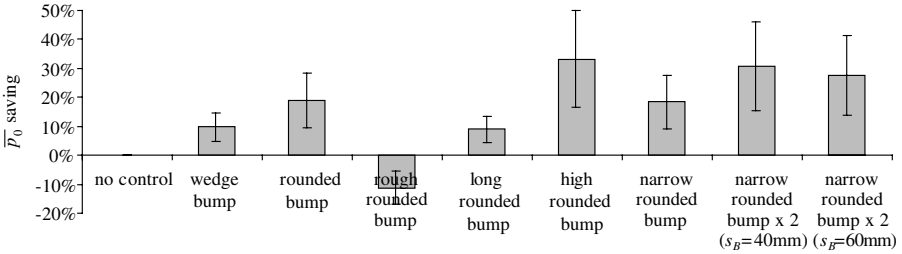

Fig. 18 Overall mass-averaged total pressure savings.

Mass-averaged total pressure savings are evaluated by the following equation, in comparison with the uncontrolled case, and plotted in Fig. 18 for each configuration. (The mass-averaged total pressure savings are subject to a large degree of uncertainty, because it quantifies the ratio of a total pressure gain with control to a total pressure loss without control, both of which are substantially small quantities for most of the tested configurations. The typical uncertainty is estimated to be up to an order of $\pm 50\%$ with an uncertainty of $\pm 1\%$ in the mass-averaged total pressure taken into account, as indicated by error bars in Fig. 18. However, the tendency of the results plotted here reasonably agrees with the characteristics of the flowfields observed and discussed in the previous Sec. VI, thus allowing qualitative evaluation of control performance.)

$$\overline{p_0}_{\text{ saving}} = \frac{\overline{\Delta p_{0\text{nc}}} - \overline{\Delta p_0}}{\overline{\Delta p_{0\text{nc}}}}, \quad \text{where } \overline{\Delta p_0} \equiv p_{01} - \overline{p_0} \qquad (2)$$

The rough rounded bump incurs large losses which can be attributed to viscous penalty from a thick boundary layer, which counterbalances the λ-shock benefit. The double configurations with the narrow rounded bumps show remarkable total pressure savings. The highest total pressure saving is marked by the high rounded bump. However, it should be noted that the mass-averaged total pressure underestimates total pressure losses in low-speed regions and separation bubbles, where the boundary-layer traverse is unable to measure negative velocity. The wedge, default rounded, narrow rounded bumps are commonly found to conduce to respectable total pressure savings.

3. Boundary-Layer Thickness

The boundary-layer growth through the SBLI is a useful indicator of viscous drag as a result of control. Spanwise averages of boundary-layer thicknesses are plotted in Fig. 19. Moderate thickening is commonly seen for most types of bump control, except for the high rounded bump which exhibited significant separation. Narrow rounded bumps are found to have gentle effects on the boundary layers. The rough rounded bump shows thicker boundary layers than the smoothed default rounded bump, but the long rounded bump has somewhat mitigated the thickening. Because most bumps investigated here have considerably rough surfaces, it can be hypothesized that smoothly manufactured bump control would incur less viscous drag than seen here.

B. Characteristics of Flowfield

1. Influence of Shock Position

For all bump shapes it was observed that the shock structure largely depends on the shock position. Figure 20 shows schematic diagrams of λ-shock structures observed with different shock positions. When the shock structure is positioned upstream (Fig. 20a), the flow is reaccelerated due to convex curvature at the front of the bump ridge in conjunction with the contraction effect due to the increasing cross-sectional area of the bump behind the main λ-shock system. Consequently a second supersonic region similar to a so-called "supersonic tongue" emerges behind the main λ-shock structure and this can result in an undesirable secondary λ-shock system and thus increase wave drag. On the other hand, Fig. 20c suggests that a λ-shock structure positioned downstream can suffer from another type of reacceleration; the supersonic flow in the λ region becomes faster due to reexpansion at the front bump ridge and leads to another shock system, which hastens boundary-layer separation, resulting in a secondary bifurcated shock system on the bump crest and boundary-layer thickening, both of which cause extra total pressure losses. Therefore it can be concluded that the shock position described in Fig. 20b is the optimum in that it can benefit from the largest possible λ-shock structure without incurring additional total pressure losses either from secondary shock systems

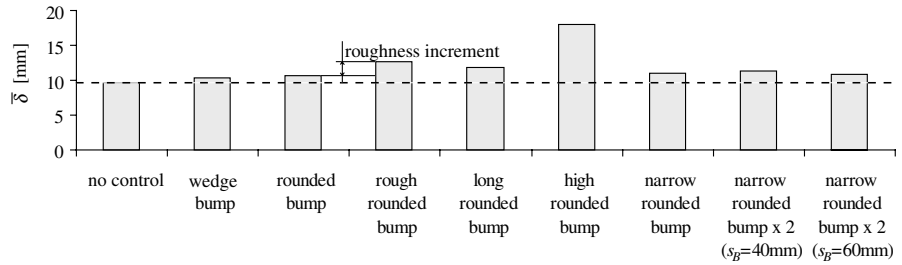

Fig. 19 Mean boundary-layer thickness.

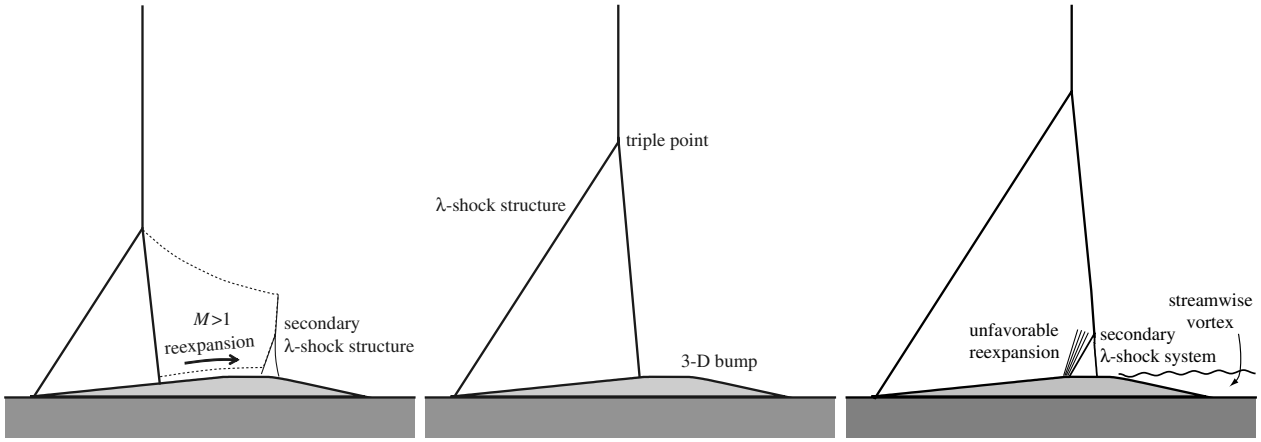

a) Front shock position **b) Optimum shock position** **c) Back shock position**

Fig. 20 λ-shock structures with various shock positions.

or boundary-layer thickening, and thus a transonic aerofoil effectively incurs minimum wave drag without additional viscous drag penalty. However, particular care must be taken in the optimization of a bump configuration for a transonic wing, because the overall performance of control should be assessed not only in terms of drag but also with respect to lift and buffet onset, as mentioned previously.

2. Features of Bump-Controlled Flow

Figure 21 is a schematic diagram of a SBLI controlled by a three-dimensional rounded bump, incorporating major features deduced from the results. Note that it depicts a case where streamwise vortices have been generated as a result of three-dimensional separation under an off-design condition, as observed in the results from computation and suggested by the vorticity in Fig. 12b. Two pairs of streamwise vortices have often been observed in oil flow patterns or boundary-layer parameter distributions in the presence of large adverse pressure gradient. In this event the resultant flow structure typically falls into the owl-face-of-the-second-kind topology defined by Perry [26], where two counter-rotating streamwise vortex pairs A and B interact with each other. The edge of the boundary layer downstream of the λ-shock structure is presented over the streamwise vortices, inferred from boundary-layer parameter distributions.

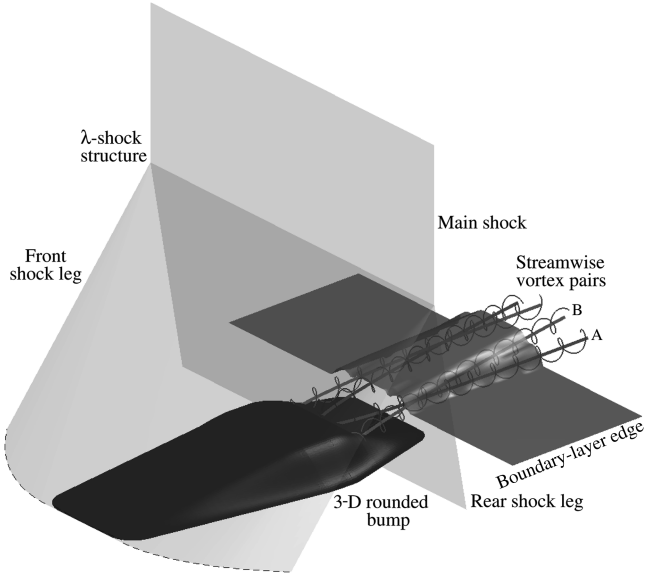

Fig. 21 Features of 3-D-rounded-bump-controlled SBLI with separation.

Streamwise vortices are expected to be beneficial in the event of imminent separation downstream of the SBLI, acting like vortex generators. Although one would avoid separation on bumps at the design point, streamwise vortices may well appear under off-design conditions as a result of separation. Therefore the complete aerofoil must be taken into account for a full evaluation of off-design performance, where losses at the bump may well be recouped elsewhere. The current computation study has revealed that the three dimensionality of the flowfield can have a considerable impact on the overall performance in various aspects such as induced drag due to spanwise lift variations and wall-normal variations of total pressure losses. These effects will be discussed in a following paper [23], as they are beyond the scope of this paper.

VI. Conclusions

The effects of various three-dimensional bumps on SBLIs have been investigated experimentally and numerically at $M_1 = 1.3$. All tested configurations have produced a fairly two-dimensional λ-shock structure which can reduce wave drag effectively. The influence of bumps on the boundary layer has been found to vary considerably, depending on the bump geometry and relative shock position. Streamwise vortices have been observed as a result of local flow separation in some cases where abrupt flow change is introduced by several factors such as angular edges and downstream movement of the shock. However, the growth of these vortices is found to be restricted within a fairly narrow region in the vicinity of the centerline and the floor. Furthermore, they have a potential to prevent large-scale separation, acting just as vortex generators. Computational simulation of a default rounded bump array on a transonic aerofoil showed a similar shock structure to that observed experimentally. The optimum shock position in terms of drag reduction has been found to be such that the rear shock foot lies at the downstream end of the bump crest in order to maximize the λ-shock benefit without incurring a large viscous penalty. In fact, thinner and fuller boundary layers have been observed for shock positions upstream of this optimum position [15], which demonstrates the robustness of three-dimensional bump control as long as the shock position is held upstream of the optimum. A double configuration of narrow rounded bumps with a relatively wide spacing $s_B/\delta_1^* \sim 60$ has been found to perform most favorably among all tested configurations, producing appreciably high total pressure recovery with the boundary layer nearly unaffected by the presence of bumps. It can be expected that greater control benefits would be obtained with smooth bump surfaces. This could not be confirmed here due to technical and budgetary restrictions.

Further investigation by means of a simple experiment or computation in channel flow is proposed to elucidate the correlation between the bump geometry and the flow deflection angle across the front shock leg. This correlation can then be used to find appropriate

bump configurations to achieve target flow deflection on a transonic aerofoil, which can be obtained with an analytical method [25] developed before the current work. Experiments should be conducted on a transonic aerofoil or wing fitted with the designed bumps in order to verify control effectiveness.

Acknowledgment

Hideaki Ogawa is thankful to the Nakajima Foundation for their financial support. Martin Pätzold gratefully acknowledges the funding for the project "Aerodynamische Auslegung und Optimierung adaptiver Stosskontrollmechanismen für transsonische Flugzeugkonfigurationen" of the Deutsche Forschungsgemeinschaft (DFG) under contract LU 809/1-1. The authors are grateful to Dave Martin and Ben Stock for the unfailing operation of the supersonic wind tunnel and Alistair Ross and Jeremy Penfold for the manufacture of experimental models.

References

[1] Pearcey, H. H., "Shock-Induced Separation and Its Prevention by Design and Boundary Layer Control," *Boundary Layer and Flow Control*, Pergamon Press, New York, Vol. 2, 1961, pp. 1166–1344.

[2] Lin, J. C., "Review of Research on Low-Profile Vortex Generators to Control Boundary-Layer Separation," *Progress in Aerospace Sciences*, Vol. 38, Nos. 4–5, May–July 2002, pp. 389–420. doi:10.1016/S0376-0421(02)00010-6

[3] Seifert, A., and Pack, L. G., "Oscillatory Control of Shock-Induced Separation," *Journal of Aircraft*, Vol. 38, No. 3, 2001, pp. 464–472.

[4] Délery, J., "Shock Wave/Turbulent Boundary Layer Interaction and its Control," *Progress in Aerospace Sciences*, Vol. 22, No. 4, 1985, pp. 209–280. doi:10.1016/0376-0421(85)90001-6

[5] Stanewsky, E., Délery, J., Fulker, J. L., and Wolfgang, G., "EUROSHOCK—Drag Reduction by Passive Shock Control," *Notes on Numerical Fluid Mechanics*, Friedrich Vieweg & Sohn Verlag, Brunswick, Germany, Vol. 56, 1997.

[6] Srinivasan, K. R., Loth, E., and Dutton, J. C., "Aerodynamics of Recirculating Flow Control Devices for Normal Shock/Boundary-Layer Interactions," *AIAA Journal*, Vol. 44, No. 4, 2006, pp. 751–763.

[7] Stanewsky, E., Délery, J., Fulker, J. L., and de Matteis, P., "EUROSHOCK II—Drag Reduction by Shock and Boundary Layer Control," *Notes on Numerical Fluid Mechanics and Multidisciplinary Design*, Springer, Berlin, Germany, Vol. 80, 2002.

[8] Smith, A. N., Babinsky, H., Fulker, J., and Ashill, P. R., "Shock-Wave/Boundary-Layer Interaction Control Using Streamwise Slots in Transonic Flows," *Journal of Aircraft*, Vol. 41, No. 3, 2004, pp. 540–546.

[9] Holden, H. A., and Babinsky, H., "Separated Shock-Boundary-Layer Interaction Control Using Streamwise Slots," *Journal of Aircraft*, Vol. 42, No. 1, 2005, pp. 166–171.

[10] Smith, A. N., Holden, H. A., Babinsky, H., Fulker, J. L., and Ashil, P. R., "Control of Normal Shock Wave/Turbulent Boundary Layer Interactions Using Streamwise Grooves," AIAA Paper 2002-0978, Jan. 2002.

[11] Holden, H. A., and Babinsky, H., "Shock/Boundary Layer Interaction Control Using 3D Devices," AIAA Paper 2003-0447, Jan. 2003.

[12] Wong, W. S., Qin, N., and Sellars, N., "A Numerical Study of Transonic Flow in a Wind Tunnel over 3D Bumps," AIAA Paper 2005-1057, Jan. 2005.

[13] Holden, H. A., "Transonic Shock/Boundary Layer Interaction Control Using Three-Dimensional Devices," Ph.D. Dissertation, University of Cambridge, Cambridge, England, U.K., 2004.

[14] Ogawa, H., and Babinsky, H., "Wind-Tunnel Setup for Investigations of Normal Shock Wave/Boundary Layer Interaction Control," *AIAA Journal*, Vol. 44, No. 11, 2006, pp. 2803–2805. doi:10.2514/1.24370

[15] Ogawa, H., "Experimental and Analytical Investigation of Transonic Shock-Wave/Boundary-Layer Interaction Control with Three-Dimensional Bumps," Ph.D. Dissertation, University of Cambridge, Cambridge, England, U.K., 2006.

[16] Pätzold, M., Lutz, T., Krämar, E., and Wagner, S., "Numerical Optimization of Finite Shock Control Bumps," AIAA Paper 2006-1054, Jan. 2006.

[17] Pätzold, M., "Auslegungsstudien von 3-D Shock-Control-Bumps mittels numerischer Optimierung," Ph.D. Dissertation, University of Stuttgart, Stuttgart, Germany, 2008.

[18] Sun, C. C., and Childs, M. E., "A Modified Wall Wake Velocity Profile for Turbulent Compressible Boundary Layers," *Journal of Aircraft*, Vol. 10, No. 6, 1973, pp. 381–383.

[19] Abernathy, R. B., Benedict, R. P., and Dowdell, R. B., "ASME Measurement Uncertainty," *Journal of Fluids Engineering*, Vol. 107, 1985, pp. 161–164.

[20] Kroll, K., Rossow, C. C., Schwmborn, D., Becker, K., and Heller, G., "MEGAFLOW—A Numerical Flow Simulation Tool for Transport Aircraft Design," *Proceedings of the 23rd ICAS Congress*, International Council of the Aeronautical Sciences, 2002.

[21] Menter, F. R., "Two-Equation Eddy-Viscosity Turbulence Models for Engineering Applications," *AIAA Journal*, Vol. 32, No. 8, 1994, pp. 1598–1605.

[22] Chung, K., "Investigation on Transonic Convex-Corner Flows," *Journal of Aircraft*, Vol. 39, No. 6, 2002, pp. 1014–1018.

[23] Pätzold, M., Lutz, T., Ogawa, H., and Babinsky, H., "Optimisation of Shock/Boundary-Layer Control with Three-Dimensional Bumps for Transonic Wings" (to be published).

[24] Ogawa, H., Babinsky, H., Pätzold, M., and Lutz, T., "Shock/Boundary-Layer Interaction Control Using Three-Dimensional Bumps for Transonic Wings," AIAA Paper 2007-0324, Jan. 2007.

[25] Ogawa, H., and Babinsky, H., "Evaluation of Wave Drag Reduction by Flow Control," *Aerospace Science and Technology*, Vol. 10, No. 1, 2006, pp. 1–8. doi:10.1016/j.ast.2005.08.001

[26] Perry, A. E., and Hornung, H., "Some Aspects of Three-Dimensional Separation, Part 2: Vortex Skeletons," *Zeitschrift für Flugwissenschaften und Weltraumforschung*, Vol. 8, No. 3, 1984, pp. 155–160.

N. Clemens
Associate Editor